Autonomous Dissipative Maxwell's Demon in a Diamond Spin Qutrit

S. Hernández-Gómez,[1,2,3,*] S. Gherardini,[1,4,5] N. Staudenmaier,[1,2,‡] F. Poggiali,[1,2,3] M. Campisi,[6,2] A. Trombettoni,[4,7] F.S. Cataliotti,[1,3] P. Cappellaro,[8] and N. Fabbri[1,3,†]

[1] *European Laboratory for Non-linear Spectroscopy (LENS), Università di Firenze, 50019 Sesto Fiorentino, Italy*
[2] *Dipartimento di Fisica e Astronomia, Università di Firenze, 50019 Sesto Fiorentino, Italy*
[3] *Istituto Nazionale di Ottica del Consiglio Nazionale delle Ricerche (CNR-INO), 50019 Sesto Fiorentino, Italy*
[4] *Scuola Internazionale Superiore di Studi Avanzati (SISSA), 34136 Trieste, Italy*
[5] *Istituto Nazionale di Ottica del Consiglio Nazionale delle Ricerche (CNR-INO), 34149 Trieste, Italy*
[6] *NEST, Istituto Nanoscienze-CNR and Scuola Normale Superiore, 56127 Pisa, Italy*
[7] *CNR-IOM DEMOCRITOS Simulation Center, 34136 Trieste, Italy*
[8] *Department of Nuclear Science and Engineering, and Department of Physics, Massachusetts Institute of Technology, Cambridge, Massachusetts 02139, USA*

(Received 8 June 2021; revised 11 January 2022; accepted 7 April 2022; published 9 May 2022)

Engineered dynamical maps combining coherent and dissipative transformations of quantum states with quantum measurements have demonstrated a number of technological applications, and promise to be a crucial tool in quantum thermodynamic processes. Here we exploit the control on the effective open spin qutrit dynamics of a nitrogen-vacancy center to experimentally realize an autonomous feedback process (Maxwell's demon) with tunable dissipative strength. The feedback is enabled by random measurement events that condition the subsequent dissipative evolution of the qutrit. The efficacy of the autonomous Maxwell's demon is quantified by means of a generalized Sagawa-Ueda-Tasaki relation for dissipative dynamics. To achieve this, we experimentally characterize the fluctuations of the energy exchanged between the system and its the environment. This opens the way to the implementation of a new class of Maxwell's demons, which could be useful for quantum sensing and quantum thermodynamic devices.

DOI: 10.1103/PRXQuantum.3.020329

I. INTRODUCTION

The Maxwell's demon paradox, introduced by Maxwell in 1867 to discuss the validity of the second law of thermodynamics, has uncovered the relationship between thermodynamics and information, and still flourishes in modern physics [1]. The demon is an intelligent entity that uses the information resulting from the measurement of a system to condition the system dynamics, with results that may be in apparent contrast with the second law of thermodynamics. One century later, Landauer and Bennett [2], the fathers of so-called information thermodynamics, provided the solution to this paradox by suggesting that one must also consider in the thermodynamic balance the information stored in the demon memory, which is erased in the process. The modern formulation of Maxwell's demons is embodied in the combination of measurement and feedback control, a typical setting of information thermodynamics [3–5]. The feedback mechanism can be either operated by an external agent or even performed internally, with no microscopic information exiting the system [6,7]. The demon can accomplish different tasks; for example, realizing information heat engines, refrigerators, thermal accelerators, or heaters [8]. In quantum settings, projective measurements contribute as a purely quantum component to heat exchange [9,10], and enable the feedback mechanism that the demon exploits to convert information into usable energy [11,12]. This feedback mechanism plays a crucial role in the investigation of quantum information thermodynamics and may find applications in an information-powered quantum refrigerator or heat engine [13,14], quantum heat transport [15], quantum computation and error correction [16], and metrology [17]. Experimental implementations of Maxwell's demons in the quantum regime have been made in an NMR setup to compensate entropy production [18], a photonic platform

*hernandez@lens.unifi.it
†fabbri@lens.unifi.it
‡Present address: Institute for Quantum Optics, Ulm University, 89081 Ulm, Germany.

working at the level of a few photons [19], superconducting QED circuits [5,20,21], solid-state spins [22], and single Rydberg atoms [23].

A Maxwell's demon generally acts via unitary evolutions; however, proper control and design of the system-environment coupling via the combination of coherent and nonunitary operations can be a fundamental resource for quantum information processing [24,25] and thermodynamics [26–28], and more broadly for quantum simulation [29] and sensing [30–32]. Dissipative operations can be used to produce quantum states of interest, such as nonequilibrium steady states and strongly correlated states, or to prepare and stabilize robust phases and entanglement [33–37]. A relevant feature of dissipative dynamics is the appearance of stationary states, not necessarily in thermal equilibrium [38,39], as a generalization of thermalization processes. Among dissipative processes, optical pumping exhibits the peculiar properties of leading the quantum system to a dissipated out-of-equilibrium state that does not depend on the system initialization. As we show, repetitive system-environment interactions via optical pumping can be modeled as an autonomous Maxwell's demon where dissipation is conditioned on the absorption of light.

Information and energy exchanges of an open quantum system with its environment inherently involve fluctuations. Quantum measurements, randomizing the system evolution, introduce quantum energy fluctuations, which impact the observable distribution obtained by averaging over many quantum trajectories [40,41]. These fluctuations can drive the quantum system toward novel—often out-of-equilibrium—dynamical regimes that could not be achieved otherwise. Quantum fluctuation relations [42,43] provide a powerful framework to characterize such energy fluctuations in thermodynamic processes. Experimental investigations of quantum fluctuation relations have been conducted recently on different platforms, including single trapped ions [44,45], NMR systems [46,47], an atom chip [48], superconducting qubits [49], nitrogen-vacancy (NV) centers in diamond [50], and entangled photon pairs [51]. These studies cover closed system dynamics [44–46,48,49], and certain open dynamics [45,47,50,51] where microreversibility may not be satisfied.

Here we realize an autonomous dissipative Maxwell's demon with a spin qutrit formed by a NV center in diamond at room temperature, and we investigate its purely quantum (non-Gibbsian) energy fluctuations through a generalized Sagawa-Ueda-Tasaki (SUT) quantum fluctuation relation. The intrinsic feedback mechanism acting on a dissipative dynamics is composed of random projective measurements followed by conditioned and tunable optical pumping. The resulting dynamics generates nonthermal steady states in the energy basis, independent of the initial state. In the case of conditioned unitary evolution, the SUT relation establishes a fundamental connection between the thermodynamic properties of nonequilibrium quantum processes and information-theoretic quantities, evaluated by measuring and manipulating the system [52–55]. The SUT relation has been generalized to completely positive trace-preserving (CPTP) maps [21,56–59]. Our work formulates such a relation in the case of conditioned dissipative dynamics and verifies it experimentally by measuring the energy change statistics of the spin qutrit. We find that expressing the SUT relation in the framework of the superoperator formalism [60] renders the computation of all the system trajectories unnecessary, drastically reducing the computational resources required . This is a relevant feature in protocols involving repeated measurements. We also measure the mean energy change of the qutrit and compare it with theoretical bounds. Finally, we find that knowledge of the stationary state is sufficient to characterize the demon in terms of its capacity for energy extraction, without requiring any additional information on the map.

This paper is structured as follows: In Sec. II we introduce the experimental platform and the implementation of the intrinsic feedback dissipative mechanism for a spin qutrit. We discuss the formalism to model the dynamics of the qutrit as an autonomous Maxwell's demon in Sec. III. Section IV contains a discussion of the SUT fluctuation relation and its extension beyond unitary dynamics. In Sec. V we present the experimental protocol to measure the energy variation of the spin qutrit due to the action of the autonomous dissipative Maxwell's demon. We also present and discuss our experimental results. A brief discussion of the energy extraction capability of dissipative demons is presented in Sec. VI. Conclusions and perspectives are summarized in Sec. VII.

II. FEEDBACK-CONTROLLED DISSIPATIVE DYNAMICS: EXPERIMENT

We now describe the intrinsic feedback dissipative dynamics realized with a diamond spin qutrit.

The negatively charged NV center, a quantum defect comprising a substitutional nitrogen atom next to a vacancy in the diamond lattice, forms an electronic spin triplet ($S = 1$) in its orbital ground state. The intrinsic electron spin-spin interaction separates in energy the state $|m_S = 0\rangle$ from the degenerate $|m_S = \pm 1\rangle$ (where $|m_S\rangle$ are the eigenstates of the spin operator $S_z = |+1\rangle\langle+1| - |-1\rangle\langle-1|$ along the NV symmetry axis z), while an applied magnetic field B aligned along z removes the degeneracy of the electronic spin states $|\pm 1\rangle$, and leads to the formation of a three-level system (3LS). Each of the three states $|m_S\rangle$ is further split into hyperfine sublevels due to coupling to the NV ^{14}N nuclear spin $I = 1$ [61]; however, we restrict our analysis to the hyperfine subspace with nuclear spin projection $m_I = +1$, since the other states are depleted as part of the initialization procedure and then are out of

resonance in the following experiments, and thus do not contribute to the spin dynamics.

The spin qutrit is coherently driven by bichromatic on-resonant microwave (MW) radiation, with frequency components $\omega_{\pm 1}$. The spin dynamics under the continuous double driving is described by the Hamiltonian $H(t) = \mathcal{H}_{\rm NV} + \omega\,[\cos(\omega_{+1}t)\,|{+1}\rangle\langle 0| + \cos(\omega_{-1}t)\,|{-1}\rangle\langle 0| + \text{h.c.}]$, where ω is the driving Rabi frequency. When ω vanishes, this Hamiltonian reduces to the intrinsic spin-1 Hamiltonian

$$\mathcal{H}_{\rm NV} = \Delta S_z^2 + \gamma_e B S_z, \tag{1}$$

where $\Delta \simeq 2.87$ GHz is the zero-field-splitting and γ_e is the electron gyromagnetic ratio ($\hbar = 1$ here and throughout this paper). When the MW driving is applied, with $\omega_{\pm 1} = \Delta \pm \gamma_e B$, in the MW rotating frame and after application of the rotating-wave approximation, the spin Hamiltonian simplifies as follows:

$$\mathcal{H}_{\rm MW} = \omega S_x. \tag{2}$$

We perform different experiments while using each of the two Hamiltonians [Eqs. (1) and (2)] to determine the unitary part of dissipative maps, and the energy basis in which fluctuations are evaluated.

On top of the unitary evolution, the system is intermittently opened by means of its interaction with a train of short laser pulses. The pulse length t_L is negligible compared with the characteristic timescale of the spin dynamics ($t_L \ll 2\pi/\omega$). Although the laser pulses are equidistant, photon absorption events follow a binomial random distribution in time, due to the finite photon absorption probability ($p_a < 1$). While a long laser pulse would produce a complete optical pumping in the $|0\rangle$ state [62], the interaction with a short laser pulse—as used here—has the following effect: If photons are not absorbed, the state of the system is unperturbed; if a photon is absorbed, the spin undergoes an optical transition to a short-lifetime orbital excited triplet state, losing any coherence in the S_z basis during the process [63], and then it decays back to the orbital ground triplet state $\{|\pm 1\rangle, |0\rangle\}$. The decay occurs through a direct spin-preserving radiative channel, or through spin-nonpreserving nonradiative

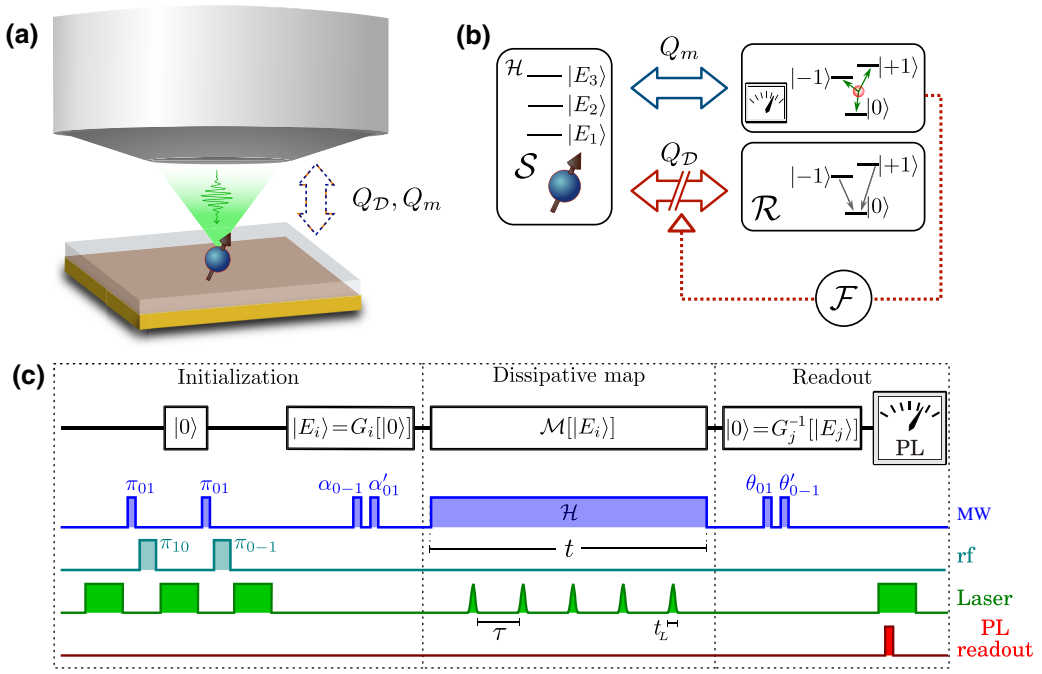

FIG. 1. (a),(b) Scheme of the spin system $\mathcal{S}$ in the presence of a green laser. On interaction with a laser pulse, the spin is subjected to a quantum measurement (Q_m) of S_z, and dissipation ($Q_{\mathcal{D}}$) toward the $m_S = 0$ spin projection. This irreversible dissipation is analogous to putting the system in contact with an out-of-equilibrium reservoir $\mathcal{R}$. Since the interaction between the system and the reservoir is conditioned by the application of a quantum measurement, the dissipation acts as an intrinsic feedback mechanism. The unitary part of the dynamics is defined by the Hamiltonian $\mathcal{H}$, with eigenstates $|E_i\rangle$, $i = 1, 2, 3$. (c) Scheme to measure energy conditional probabilities. The stochastic dissipative map $\mathcal{M}$ is a combination of a train of N_L equidistant short laser pulses and a continuous driving under the Hamiltonian $\mathcal{H}$ that can be either $\mathcal{H}_{\rm NV}$ or $\mathcal{H}_{\rm MW}$ (see the main text). The total time of the experiment $t = N_L\tau$ is defined in terms of the number of laser pulses and the time τ between them. The laser pulse duration t_L is negligible with respect to the continuous driving. The gates $G_i : |0\rangle \to |E_i\rangle$ and $G_j^{-1} : |E_j\rangle \to |0\rangle$ enable one to prepare and read out the Hamiltonian eigenstates, respectively, by exploiting the optical properties of the NV center.

paths involving intermediate metastable states. The different decay rates of the radiative and nonradiative paths result in an optical pump of the spin toward the state $|0\rangle$. Considering the reduced three-level system formed by the spin levels of the orbital ground state, the photon absorption induces a loss of coherence and an *irreversible dissipation*, originating from optical pumping. Such dissipation, conditioned by the absorption of a photon, constitutes the basis of the intrinsic feedback dissipative dynamics, as schematized in Figs. 1(a) and 1(b). The mathematical model of these phenomena is described in Sec. III.

III. MODELED DYNAMICS: AUTONOMOUS DISSIPATIVE MAXWELL'S DEMON

Here we model the qutrit dynamics in terms of a Lindbladian master equation describing an autonomous dissipative Maxwell's demon. For this we use the formalism described in Ref. [60] for superoperators represented as $N^2 \times N^2$ matrices, where $N = 3$ is the dimension of the Hilbert space of the 3LS. According to this formalism, a given density matrix ρ under unitary evolution $U \equiv e^{-i\tau\mathcal{H}}$ is transformed into

$$\mathrm{col}[U\rho U^\dagger] = \mathbf{U}\mathrm{col}[\rho], \tag{3}$$

where $\mathrm{col}[\rho]$ denotes the vectorization of ρ, obtained by stacking the columns of ρ to form a "column" vector, and $\mathbf{U} \equiv \exp[-i\tau(\mathcal{H} \otimes \mathbb{1}_{3\times3} - \mathbb{1}_{3\times3} \otimes \mathcal{H}^*)]$, with $\otimes$ being the Kronecker product.

On the other hand, the interaction between the 3LS and a short laser pulse can be described by a positive-operator-valued measure (POVM) followed by a dissipation operator conditioned on the POVM result. Specifically, the interaction with a single short laser pulse transforms a density matrix ρ into

$$\mathrm{col}[\rho(t_L)] = \boldsymbol{\mathcal{A}}\mathrm{col}[\rho], \tag{4}$$

where the superoperator $\boldsymbol{\mathcal{A}}$ models the mean effect of the single short laser pulse. Taking into account all the possible outcomes of the 3LS-laser interaction, we write $\boldsymbol{\mathcal{A}}$ as

$$\boldsymbol{\mathcal{A}} \equiv \sum_{j=1}^{4} \boldsymbol{\mathcal{D}}_j \mathbf{m}_j, \tag{5}$$

where $\mathbf{m}_j \equiv m_j \otimes m_j$ is one of the measurement superoperator associated with the POVM $m_j = \{m_1, m_2, m_3, m_4\}$, with

$$m_1 \equiv \sqrt{p_a}\,|-1\rangle\langle-1|, \tag{6a}$$

$$m_2 \equiv \sqrt{p_a}\,|0\rangle\langle0|, \tag{6b}$$

$$m_3 \equiv \sqrt{p_a}\,|+1\rangle\langle+1|, \tag{6c}$$

$$m_4 \equiv \sqrt{(1-p_a)}\mathbb{1}_{3\times3}, \tag{6d}$$

such that $\sum_{j=1}^{4} m_j m_j^\dagger = \mathbb{1}_{3\times3}$, and $\boldsymbol{\mathcal{D}}_j$ represents the action of a superoperator conditioned to the result of the POVM:

$$\boldsymbol{\mathcal{D}}_j = \begin{cases} \mathbb{1}_{9\times9} & \text{if } j = 4, \\ \boldsymbol{\mathcal{L}} & \text{otherwise,} \end{cases} \tag{7}$$

with

$$\boldsymbol{\mathcal{L}} \equiv \exp\left(t_L \sum_{\ell=0}^{1} L_\ell^* \otimes L_\ell - \frac{1}{2}\mathbb{1}_{3\times3} \otimes L_\ell^\dagger L_\ell - \frac{1}{2}(L_\ell^\dagger L_\ell)^* \otimes \mathbb{1}_{3\times3} \right), \tag{8}$$

where $(\cdot)^*$ denotes the complex conjugate and L_ℓ are the Lindblad jump operators $\{L_0, L_1\} \equiv \{\sqrt{\Gamma}\,|0\rangle\langle+1|, \sqrt{\Gamma}\,|0\rangle\langle-1|\}$, describing the dissipation toward the state $|0\rangle$. In Eq. (5), the term for $j = 4$ corresponds to the case where the laser pulse is not absorbed, while the other three terms model the absorption of a single laser pulse. The Lindblad dissipative superoperator $\boldsymbol{\mathcal{L}}$ is defined in terms of the product of the effective decay rate and the laser duration Γt_L, which dictates the strength of the dissipation that brings the system toward $|0\rangle$; the dissipation probability $p_d \equiv (1 - e^{-\Gamma t_L})$. The explicit expression for $\boldsymbol{\mathcal{L}}$ can be found in Supplemental Material [75]. Using short laser pulses with $t_L = 41$ ns, we experimentally characterize the strength of this decay rate, resulting in a value such that $\Gamma t_L \simeq 1/2$. Given the effective nature of this model, the value of Γ might differ for different NV centers and under different experimental conditions. Notice that for a long laser pulse ($t_L\Gamma \gg 1$) any given state ρ is transformed into $\boldsymbol{\mathcal{L}}\mathrm{col}[\rho] = \mathrm{col}[|0\rangle\langle0|]$, which is consistent with the usual protocol used to optically initialize the electronic spin state. Note that in the hypothetical limit where $p_d = 0$, no dissipation will occur ($\boldsymbol{\mathcal{L}} = \mathbb{1}_{9\times9}$), and consequently $\boldsymbol{\mathcal{D}}_j = \mathbb{1}_{9\times9}$.

Here, the action of the dissipation operator is conditioned on the result of the previously applied POVM. Thus, the combined effect of unitary evolution, POVMs, and dissipation results in an *autonomous Maxwell's demon*, whose action is defined by the specific photodynamics of the NV center [see Fig. 1(b)]. Overall, the effect of this feedback-controlled dissipative map $\mathcal{M}$ after N_L laser pulses is thus modeled as $\mathcal{M}[\rho] \to \boldsymbol{\mathcal{B}}^{N_L}\mathrm{col}[\rho]$, where $\boldsymbol{\mathcal{B}}$ is the superoperator that describes a single block of the dynamics formed by unitary evolution followed by the interaction of the system with a short laser pulse:

$$\boldsymbol{\mathcal{B}} \equiv \boldsymbol{\mathcal{A}}\,\mathbf{U}. \tag{9}$$

The study of energy variation fluctuations induced by this autonomous Maxwell's demon is a central issue of this article.

IV. DISSIPATIVE SAGAWA-UEDA-TASAKI RELATION

In this context, quantum fluctuation relations [43] provide a powerful framework to characterize fluctuations of energy by inspecting its characteristic function. The quantum fluctuation relation for dynamics under measurements and feedback control, also known as the quantum Sagawa-Ueda-Tasaki relation, was originally proposed for protocols where specific unitary operations are applied to the quantum system depending on the outcomes of a sequence of projective measurements [53,54]. Later it was extended to the more general case of nonunitary dynamics described by CPTP maps, subject to the result of the POVMs—which generalize the projective measurements [21,56–59]. Here we detail how to formulate such an extension using the superoperator formalism, instead of the usual Kraus operator formalism.

A two-point-measurement (TPM) scheme [64] is used to characterize the statistics of the energy variation: an initial energy measurement projects an initial thermal state ρ^{th} into one of the Hamiltonian eigenstates, which then evolves under the map we are studying, and a final energy measurement allows us to extract the energy difference. By repeating this process several times, one can reconstruct the probability distribution of the energy variation:

$$P_{\Delta E} \equiv \sum_{i,j} \delta(\Delta E - \Delta E_{j,i}) P_{j|i} P_i, \tag{10}$$

where $\Delta E_{j,i} \equiv E_j - E_i$, P_i is the probability of obtaining E_i as a result of the first energy measurement of ρ^{th}, and $P_{j|i}$ is the conditional probability of obtaining E_j as a result of the second energy measurement at the end of the TPM scheme. Once the statistics of ΔE are known, the characteristic function $\mathcal{G}(\eta) \equiv \langle e^{iu\Delta E} \rangle_{u=i\eta}$ of $P_{\Delta E}$ can be experimentally computed as

$$\mathcal{G}(\eta) = \sum_{i,j} e^{-\eta \Delta E_{j,i}} P_{j|i} P_i. \tag{11}$$

The general protocol is as follows. An n-dimensional quantum system (in our experiments, $n = 3$) evolves under the Hamiltonian H_0; then a POVM measurement is performed on the system. The quantum measurement is defined by a set of positive semidefinite operators $\Pi_1, \ldots, \Pi_{n'}$ such that $\sum_{k=1}^{n'} \Pi_k = \mathbb{1}_{n\times n}$. According to a feedback mechanism, the measurement outcome k determines the CPTP map Φ_k under which the system continues to evolve. Since Φ_k is a CPTP map, we can define the superoperator propagator $\mathbf{\Phi}_k$ such that the evolution of a generic density matrix ρ is described as $\text{col}[\Phi_k[\rho]] = \mathbf{\Phi}_k \text{col}[\rho]$ [60]. Hence, the complete feedback map $\mathcal{M}_\Phi$ transforms the density matrix ρ into

$$\text{col}[\mathcal{M}_\Phi[\rho]] = \sum_{k=1}^{n'} \mathbf{\Phi}_k \mathbf{\Pi}_k \mathbf{U}_0 \text{col}[\rho], \tag{12}$$

where $\mathbf{U}_0 = \exp[-it(H_0 \otimes \mathbb{1}_{n\times n} - \mathbb{1}_{n\times n} \otimes H_0^*)]$ is the superoperator that describes the unitary evolution before the POVM, and $\mathbf{\Pi}_k \equiv \Pi_k \otimes \Pi_k$ represents the action of the measurement operators on the quantum system.

As a result, the characteristic function of the energy variation is equal to a parameter γ that represents the efficacy of the feedback mechanism:

$$\mathcal{G}(\beta) = \gamma \equiv \sum_{k=1}^{n'} \text{Tr}_{n\times n} \left[\mathbf{\Pi}_k^\dagger \mathbf{\Phi}_k^\dagger \, \text{col}[\rho_{\text{f}}^{\text{th}}] \right], \tag{13}$$

where β is the inverse temperature of the initial thermal state, ρ_f^{th} is a thermal state at the final time of the TPM scheme, the symbol † denotes conjugate-transpose, and $\text{Tr}_{n\times n}[\text{col}[\cdot]] \equiv \text{Tr}[\cdot]$. The efficacy of the feedback mechanism, as measured by $-\ln\gamma$, determines a lower bound on the energy variation of the system, as we discuss in Sec. VI. The mathematical proof of Eq. (13) can be found in Appendix A (see Corollary 1). The proof is based on the fact that the map $\mathcal{M}_\Phi$ is itself a CPTP map, meaning that Eq. (13) is a particular case of the general quantum fluctuation relation for CPTP maps [21,56–59,65]. It is worth observing that Eq. (13) reduces to the original quantum SUT relation [53] in the particular case where the intermediate quantum measurements are projective and Φ_k are unitary evolution operators. Moreover, if Φ_k are unital CPTP maps, then $\mathbf{\Phi}_k^\dagger$ is trace preserving [60], and hence $\gamma = 1$ [56,58] for any time-independent Hamiltonian. In contrast, for nonunital maps where microreversibility is not satisfied, the value of γ can be different from 1 and, in general, involves non-trace-preserving operators $\mathbf{\Phi}_k^\dagger$.

Equations (12) and (13) refer to a feedback operation on the quantum system enabled by applying a single POVM measurement, and they can be simplified by defining $\mathcal{B}_\Phi \equiv \sum_{k=1}^{n'} \mathbf{\Phi}_k \mathbf{\Pi}_k$, which leads to $\gamma = \text{Tr}_{n\times n}[\mathcal{B}_\Phi^\dagger \, \text{col}[\rho^{\text{th}}]]$. Therefore, extending the protocol to the scenario where measurements and feedback are applied repeatedly is quite straightforward: after N repetitions, $\gamma = \text{Tr}_{n\times n}[(\mathcal{B}_\Phi^\dagger)^N \, \text{col}[\rho^{\text{th}}]]$. Expressing γ in this way significantly simplifies its computation, because it removes the requirement to calculate every possible quantum trajectory originating from the system dynamics; compare this, for example, with Refs. [15,53]. This advantage may be significant since the number of trajectories scales exponentially with the number of measurements. In addition, for any CPTP dissipative map, whereby the system asymptotically reaches the single steady state $\text{col}[\rho^\infty] \equiv \lim_{N\to\infty} (\mathcal{B}_\Phi)^N \text{col}[\rho]$, for a generic initial state ρ, we can

write the asymptotic value of γ as (see also Corollary 2 in Appendix A)

$$\gamma^{\infty} \equiv \lim_{t\to\infty} \gamma = n\langle \rho^{\infty}, \rho^{\text{th}} \rangle_{\text{HS}} \tag{14}$$

where $\langle \rho_1, \rho_2 \rangle_{\text{HS}} \equiv \text{Tr}[\rho_1^{\dagger}\rho_2]$ denotes the Hilbert-Schmidt inner product, and n is the dimension of the quantum system. Remarkably, the quantity in Eq. (14) can be measured experimentally, even for nonunital maps.

V. DYNAMICS AND THERMODYNAMICS OF THE DEMON

We characterize the dynamics and the quantum (nonthermal) energy fluctuations of the three-level spin system induced by nonunital quantum dissipative maps in two independent experiments:

1. Coherent double driving and short laser pulses. The unitary part of the map $\mathcal{M}$ is ruled by the Hamiltonian $\mathcal{H}_{\text{MW}}$ defined in Eq. (2), with eigenstates $|E_1\rangle = |-\omega\rangle$, $|E_2\rangle = |\emptyset\rangle$, and $|E_3\rangle = |+\omega\rangle$, where $|\pm\omega\rangle \equiv 1/2\left(|-1\rangle \pm \sqrt{2}\,|0\rangle + |1\rangle\right)$ and $|\emptyset\rangle \equiv 1/\sqrt{2}\,(|-1\rangle - |1\rangle)$.
2. Undriven spin, subject to short laser pulses. The spin Hamiltonian is $\mathcal{H}_{\text{NV}}$ with eigenstates $|E_1\rangle = |0\rangle$, $|E_2\rangle = |-1\rangle$, and $|E_3\rangle = |+1\rangle$.

The effect of the map $\mathcal{M}$ on the spin energy is characterized by measuring the energy jump probabilities; that is, the conditional probabilities associated with the energy variation in a given time interval. The scheme used to measure conditional probabilities, as depicted in Fig. 1(c), consists of the following steps:

(a) Initialize the system into one of the Hamiltonian eigenstates, say, $|E_i\rangle$.
(b) Evolve the system under the map $\mathcal{M}$ up to time t.
(c) Read out the probability of the spin being in the Hamiltonian eigenstate $|E_j\rangle$ at final time t.
(d) Repeat the procedure for each initial and final Hamiltonian eigenstate.

A. Spin initialization and readout

The NV spin is initially prepared in the spin qutrit Hamitonian eigenstate $|E_i\rangle$. The starting point of the initialization is a thermal spin mixture $\overline{\rho} = \sum_{m_S,m_I} |m_S, m_I\rangle\langle m_S, m_I|$ within the 9×9 space described by the hyperfine manifold within the orbital ground state. The quantum gate G_0 prepares the hyperfine state $|m_S, m_I\rangle \equiv |0, 1\rangle$ (see Fig. 1). From now on we drop the hyperfine spin to simplify the notation, $|m_S, 1\rangle = |m_S\rangle$. The details of the nuclear spin initialization can be found in Supplemental Material [75]. Pure electron spin states in the energy basis ($|E_i\rangle$) are then prepared by applying opportune two-level-system quantum gates (G_i in Fig. 1). These gates are realized by means of nuclear spin selective monochromatic microwave pulses resonant with the electronic transition $|0\rangle \to |+1\rangle$ or $|0\rangle \to |-1\rangle$ as described in Appendix B.

After a spin evolution under the dissipative map $\mathcal{M}$, we readout the spin state by exploiting the difference in the photoluminescence (PL) intensity of the NV center, among state $|0\rangle$ and states $|\pm 1\rangle$, upon illumination with green laser light. To measure the probability of the spin state being equal to each of the three Hamiltonian eigenstates $|E_j\rangle$ at the end of the protocol, that eigenstate is projected into the S_z eigenstate $|0\rangle$ (quantum gate G_j^{-1} in Fig. 1), and then the PL intensity is recorded. The description of the gates G_i and G_j^{-1} for each of the initial and final eigenstates can be found in Appendix B. Since the readout process is destructive, each experiment is composed of three different runs, where the probability of each of the three eigenstates is recorded. Because of the limited diamond PL collection efficiency and photon shot noise, each experiment is repeated approximately 10^6 times.

Notice that the duration of each realization of the experiment is much shorter than the nuclear spin lifetime, so the three-dimensional hyperfine spin subspace is well defined for the whole duration of the experiment.

B. Demon dynamics

We then reconstruct the dynamics of the spin qutrit under the autonomous dissipative Maxwell's demon. The conditional probabilities $P_{j|i}$ associated with energy jumps from the initial ($|E_i\rangle$) to the final ($|E_j\rangle$) eigenstates are shown in Fig. 2 as a function of the number of laser pulses applied before the readout is performed. The experimental data are shown together with the theoretical model of the dynamics, described in Sec. III. The excellent agreement between experiment and theory leads us to conclude that the dynamics of the system is very well described by an autonomous feedback mechanism. The results show that the conditional probabilities $P_{j|i}$ tend to a single constant value in the long-time regime (large N_L). In other words, the spin state asymptotically approaches a *steady state in the energy basis* (SSE) that does not depend on the initial state, thus confirming the dissipative nature of the map $\mathcal{M}$. In the case of $\mathcal{H} = \mathcal{H}_{\text{NV}}$ [Fig. 2(b)], the asymptotic state is $\rho_{\text{NV}}^{\infty} = \sum_{\ell=-1}^{+1} p_{\ell}^{\infty} |\ell\rangle\langle\ell|$, with populations, obtained from the experimental data, $p_{+1}^{\infty} = -0.01 \pm 0.01$, $p_0^{\infty} = 1.01 \pm 0.01$, and $p_{-1}^{\infty} = 0.00 \pm 0.01$. In such a case, the protocol is asymptotically equivalent to an initialization procedure into $\rho_{\text{NV}}^{\infty} = |0\rangle\langle 0|$. On the other hand, if $\mathcal{H} = \mathcal{H}_{\text{MW}}$ [Fig. 2(a)], the asymptotic state significantly differs from $|0\rangle = 1/\sqrt{2}\,(|+\omega\rangle - |-\omega\rangle)$. Although the interaction with each laser pulse pushes the system toward $|0\rangle$, the unitary evolution modifies the density operator populations in

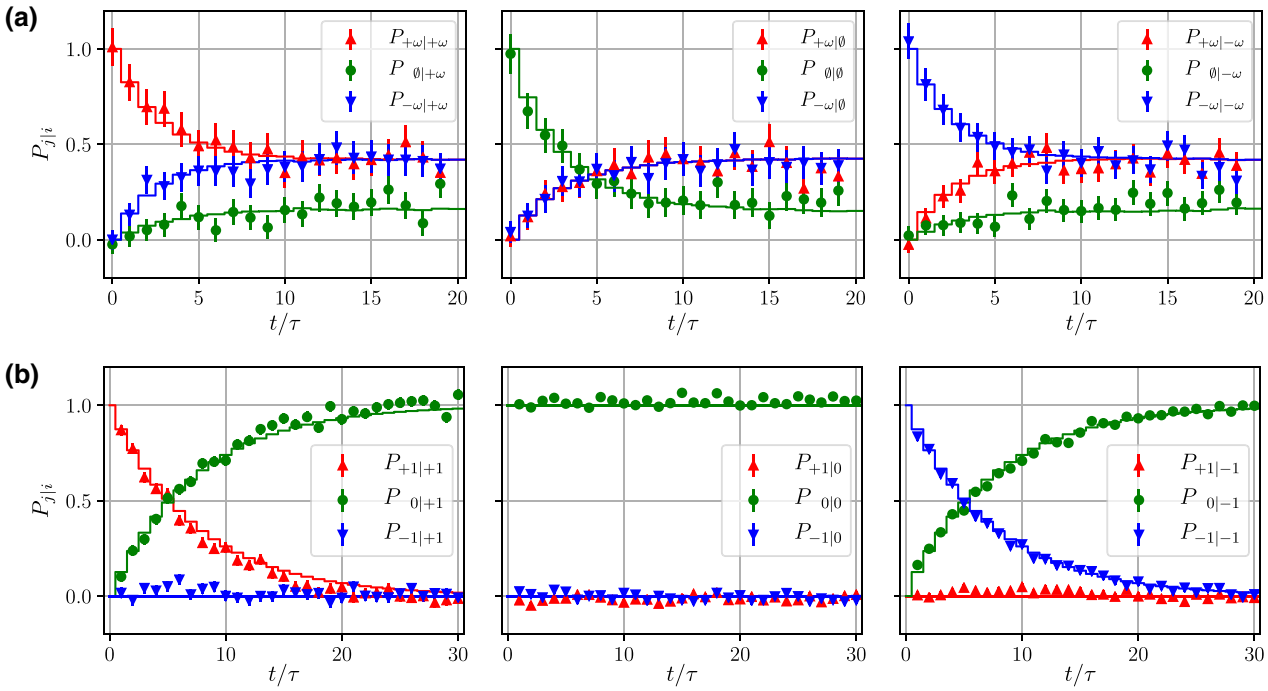

FIG. 2. Dynamics of the spin qutrit under the autonomous dissipative Maxwell's demon. The probability $P_{j|i}$ of measuring the state $|E_j\rangle$ after applying the map $\mathcal{M}$ to the state $|E_i\rangle$ is shown as a function of the number of laser pulses $N_L = t/\tau$, where $|E_i\rangle$ and $|E_j\rangle$ represent each of the eigenstates of the 3LS Hamiltonian (a) $\mathcal{H}_{\mathrm{MW}}$ and (b) $\mathcal{H}_{\mathrm{NV}}$. In both cases, the duration of the laser pulses $t_L = 41$ ns, and the time between pulses $\tau = 424$ ns. Each panel corresponds to a different initial eigenstate: (a) $\{|+\omega\rangle, |\emptyset\rangle, |-\omega\rangle\}$ and (b) $\{|+1\rangle, |0\rangle, |-1\rangle\}$. The markers with error bars represent the experimental data, and each solid line corresponds to the calculation performed with the theoretical model of the map $\mathcal{M}$, as described in Sec. III. Experimental error bars are mainly due to photon shot noise. Notice that these measurement stem from a comparison between the PL of the two reference states and the PL of the NV center after the studied dynamics, which may result in values that are slightly outside the interval [0, 1].

the S_z basis, thus changing the SSE at long times. In such a case, the asymptotic state is $\rho^{\infty}_{\mathrm{MW}} = \sum_{\ell=-\omega}^{+\omega} p^{\infty}_{\ell} |\ell\rangle\langle\ell|$, with populations, obtained from the experimental data, $p^{\infty}_{+\omega} = 0.41 \pm 0.01$, $p^{\infty}_{\emptyset} = 0.20 \pm 0.02$, and $p^{\infty}_{-\omega} = 0.40 \pm 0.01$, as shown in Fig. 2(a).

C. Energy variation distribution

On the basis of the formalism established in Sec. IV, here we study the statistics of the energy exchange fluctuations of the demon and we calculate the feedback efficacy for the specific map $\mathcal{M}$.

For an initial thermal state, measuring the conditional probabilities $P_{j|i}$ gives access to the probability distribution of the energy variation $P_{\Delta E}$, as defined in Eq. (10). We recall that in the usual TPM scheme [64], the probability P_i is measured by performing an energy projective measurement on the initial state. Here we initialize the spin into each of the eigenstates of the Hamiltonian [Sec. V], and we obtain mixed (equilibrium) states as a statistical mixture of the eigenstates with probabilities P_i as weight factors. Our scheme gives results equivalent to those given by a TPM scheme, owing to the large number of experimental realizations [50,66], while overcoming the difficulties to prepare an initial thermal state. Moreover, our scheme removes possible experimental errors inherent in the first energy measurement, and allows one to use a single set of measurements to study different initial states.

Once we have measured the energy variation distribution $P_{\Delta E}$, we can experimentally compute the values of the characteristic function $\mathcal{G}(\eta)$ as in Eq. (11). In addition, as pointed out in Sec. IV, the value of γ^{∞} can be independently computed from the initial and asymptotic states of the map [Eq. (14)]. The measurements of $\mathcal{G}(\beta)$ and γ^{∞} are shown in Fig. 3. The agreement between the measured values of these two parameters represents the experimental verification of the generalized SUT fluctuation relation [Eq. (13)], in the SSE regime, for an open three-level system under quantum (nonthermalizing) dissipative dynamics conditioned by POVM quantum measurements. We note that the theoretical model of the map $\mathcal{M}$ [Sec. III] allows us to calculate the efficacy γ also in the transient regime, as

$$\gamma = \mathrm{Tr}_{3\times 3}\left[(\mathcal{B}^{\dagger})^{N_L}\,\mathrm{col}[\rho^{\mathrm{th}}]\right], \tag{15}$$

with $\mathcal{B}$ defined in Eq. (9). Here it is worth noting that the "backwards" superoperator $\mathcal{B}^{\dagger}$ is not trace preserving, a

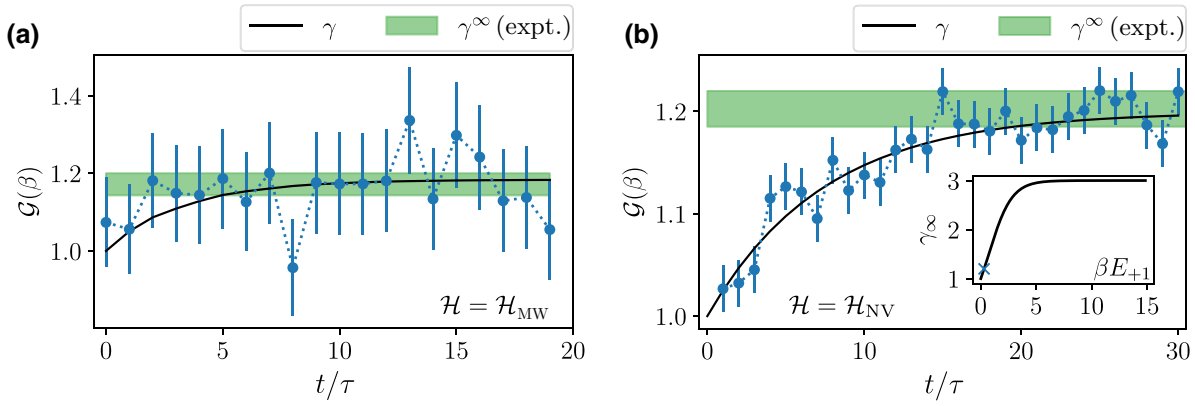

FIG. 3. Experimental verification of the generalized quantum Sagawa-Ueda-Tasaki relation (13) for a 3LS controlled by an autonomous dissipative Maxwell's demon. The energy variation statistics are shown in terms of the total time of the experiment divided by the time between laser pulses (i.e., in terms of the number of laser pulses $N_L = t/\tau$). (a) The continuous coherent driving of the 3LS is defined by the Hamiltonian $\mathcal{H}_{\rm MW}$, and the value of the inverse temperature of the initial state is given by $\beta = 3/E_{+\omega}$. (b) Same as (a) but for a Hamiltonian $\mathcal{H}_{\rm NV}$, and an inverse temperature of the initial state $\beta = 0.297/E_{+1}$. Blue circles represent the measured values of the characteristic function $\mathcal{G}(\beta)$, the continuous black line denotes the theoretical estimation of γ [Eq. (15)], and the green area marks the experimental value of γ^∞ [Eq. (14)], the asymptotic value of γ. The inset shows the theoretical value of γ^∞ as a function of the initial inverse temperature β. The blue cross is associated with the value of β used for the experimental data in (b).

clear sign of the nonreversibility associated with the dissipative process [15]. In the transient regime, the values of γ [Eq. (15)] are compared with the experimental values of the characteristic function $\mathcal{G}(\beta)$, as a function of the number of laser pulses. As shown in Figs. 3(a) and 3(b), there is excellent agreement between the two quantities.

In the specific case of $\mathcal{H} = \mathcal{H}_{\rm NV}$, where the Hamiltonian commutes with the POVM operators and with the dissipative operator, we can derive an analytic expression for the efficacy γ defined in Eq. (15) as

$$\gamma = \mu^{N_L} + 3(1-\mu^{N_L})e^{\beta F}, \tag{16}$$

where $F \equiv -\beta^{-1}\ln Z$ is the initial free energy of the system, with $Z \equiv \sum_{k=-1}^{1} e^{-\beta E_i}$, and $\mu \equiv 1 - p_d p_a \in [0,1]$ defines the probability of the system not being subjected to feedback. We also recall that p_a denotes the laser pulse absorption probability, and $p_d \equiv (1 - e^{-t_L\Gamma})$ is the dissipation probability for the interaction with a single laser pulse (Sec III). The derivation of Eq. (16) is given in Supplemental Material [75]. As one would expect, $\gamma = 1$ if $p_a = 0$ (closed quantum system), or in the case of pure projective measurements without dissipation, $e^{-t_L\Gamma} = 1$ (no feedback). In addition, since $Z < 3$ for $\beta \neq 0$, Eq. (16) implies that $\gamma > 1$, a necessary condition for energy extraction [15] (see also Sec. VI). As a final remark, notice that γ in Eq. (16) is defined in terms of macroscopic quantities—it does not depend on the trajectories followed by the system. In the inset in Fig. 3(b), we show the behavior of the asymptotic value of $\gamma^\infty = 3\,e^{\beta F}$ obtained from Eq. (16) in the SSE regime as a function of the inverse initial temperature β. This result is in agreement with Eq. (14) for the asymptotic state $\rho_{\rm NV}^\infty = |0\rangle\langle 0|$.

VI. EXTRACTABLE ENERGY IN AUTONOMOUS DISSIPATIVE DEMONS

In this section, we characterize the Maxwell's demon in terms of its capability of energy extraction.

The mean energy variation originating from the demon is defined as $\langle \Delta E\rangle \equiv \int \Delta E P_{\Delta E}\, d\Delta E$, which can be rewritten as $\langle \Delta E\rangle = \sum_{i,j}(E_j - E_i)P_{j|i}P_i$ using Eq. (10). Negative values of $\langle \Delta E\rangle$ denote the extraction of energy from the system. The maximal amount of extractable energy $(-\langle \Delta E\rangle)$ is expected to be bounded from above [15,53] by two fundamental quantities, $\ln\gamma$ and the classical *mutual information* $\mathcal{I}$, which measures the degree of correlation between the actual outcomes of the POVMs and the outcomes recorded by the demon. In the case of an autonomous demon—where no microscopic information needs to be read out by an external agent during the feedback process—no errors are associated with the intermediate measurements. In this error-free limit the mutual information $\mathcal{I}$ reduces to the Shannon entropy [53] (i.e., the measurement of the degree of correlation between the trajectories of the system). For a quantum dynamics under the action of measurements and feedback, each sequence of measurements $(k_1,\ldots,k_{N_L})$ corresponds to a different quantum trajectory. Thus, formally one has in the error-free limit

$$\begin{aligned}\mathcal{I} &\longrightarrow \langle S_{k_1,\ldots,k_{N_L}}\rangle \\ &= -\sum_{k_1,\ldots,k_{N_L}} p(k_1,\ldots,k_{N_L})\ln p(k_1,\ldots,k_{N_L}),\end{aligned} \tag{17}$$

where $\langle S_{k_1,\ldots,k_{N_L}}\rangle$ is the Shannon entropy, and $p(k_1,\ldots,k_{N_L})$ is the probability of the system following the $(k_1,\ldots,k_{N_L})$

trajectory. This probability is defined as

$$p(k_1,\ldots,k_{N_L}) = \mathrm{Tr}_{n\times n}[\mathbf{m}_{k_{N_L}}\mathbf{U}\mathcal{D}_{k_{N_L-1}}\mathbf{m}_{k_{N_L-1}}\mathbf{U}\cdots \cdots \mathcal{D}_{k_1}\mathbf{m}_{k_1}\mathbf{U}\,\mathrm{col}[\rho^{\mathrm{th}}]], \tag{18}$$

where each k_i can take the values $\{1,2,3,4\}$, which indicate one of the results of the ith POVM, as described by Eqs. ((6a))–(6d).

In Fig. 4 we compare the experimental values of $\beta\langle\Delta E\rangle$ (with fixed inverse temperature $\beta > 0$) with the calculated values of $-\ln\gamma$ and $-\mathcal{I}$ as a function of the number of laser pulses. Note that the number of trajectories grows as 4^{N_L}; therefore, the exact estimation of $\mathcal{I}$ becomes impractical for large N_L. In Fig. 4 we show the exact values of $-\mathcal{I}$ for $N_L < 10$ (up to approximately 2.6×10^5 trajectories). In contrast, $\langle\Delta E\rangle$ and γ do not require the computation of single trajectories, since they are determined simply in terms of $\mathcal{B}^{N_L}$ and $(\mathcal{B}^\dagger)^{N_L}$, respectively. In the case where $\mathcal{H} = \mathcal{H}_{\mathrm{MW}}$, energy extraction does not occur (indeed, $\beta\langle\Delta E\rangle > 0$). In contrast, in the case $\mathcal{H} = \mathcal{H}_{\mathrm{NV}}$, $\beta\langle\Delta E\rangle < 0$ for any time $t > 0$. Moreover, one can observe that even experimentally the inequality

$$\beta\langle\Delta E\rangle \geq \max\left\{-\ln\gamma, -\langle S_{k_1,\ldots,k_{N_L}}\rangle\right\} \tag{19}$$

is always validated for any value of t. However, in both experimental scenarios, the tightest bound is provided by $\ln\gamma$.

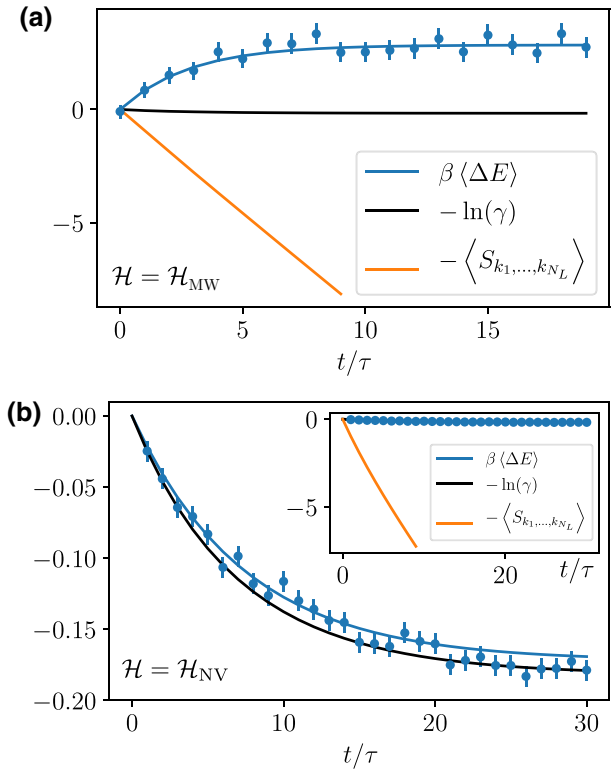

FIG. 4. Experimental values of $\beta\langle\Delta E\rangle$ as a function of the number of laser pulses for a 3LS with Hamiltonian operators $\mathcal{H}_{\mathrm{MW}}$ (a) and $\mathcal{H}_{\mathrm{NV}}$ (b). Negative values of $\beta\langle\Delta E\rangle$ (with $\beta > 0$) may allow energy extraction from the 3LS. The solid blue line corresponds to the values of $\beta\langle\Delta E\rangle$ as predicted by theory, while the theoretical bounds $-\ln\gamma$ and $-\langle S_{k_1,\ldots,k_{N_L}}\rangle$ are denoted by solid black and orange lines, respectively. The inset in (b) shows at the same time the tightness of $-\ln\gamma$ and the discrepancy of $-\langle S_{k_1,\ldots,k_{N_L}}\rangle$, both with respect to the mean energy variation $\beta\langle\Delta E\rangle$.

We now analyze the task of energy extraction in stationary conditions. Implementing the intrinsic feedback mechanism of the demon by means of dissipative operations implies that the quantum system asymptotically reaches a SSE (i.e., a state for which, on average, the open system does not exchange energy with the external environment) despite the active presence of interaction dynamics (indeed, the quantum system is not closed). In the SSE regime, the energy jump conditional probabilities are independent of the initial state, and this entails that $\lim_{t\to\infty} P_{j|i}(t) = p_j^\infty$, as shown in Sec. V B. Therefore, in such a regime the mean energy variation is time independent and depends only on the difference between the mean energy of the asymptotic and initial states: $\langle\Delta E\rangle = \langle E\rangle_\infty - \langle E\rangle_0$, where $\langle E\rangle_\infty \equiv \mathrm{Tr}[\rho^\infty H] = \sum_j p_j^\infty E_j$ and $\langle E\rangle_0 \equiv \mathrm{Tr}[\rho^{\mathrm{th}} H]$. This requires knowledge of only the initial state and the measurement of the stationary state ρ^∞ induced by dissipation (or more precisely, the measurement of the stationary populations of the system, since the TPM scheme projects the final state into the energy basis of the 3LS). Notice that although the SSE is independent of the initial state, it does depend on the parameters that determine the feedback-controlled quantum map. For example, for the demon that we realize, in the limit of vanishing dissipation ($p_{\mathrm{d}} \to 0$, i.e., unital dynamics) the SSE would be a completely mixed state, with no possibility to extract energy. More broadly, the sign and the value of the energy change might be arbitrarily tuned by a careful choice of the setup parameters.

In Fig. 5 we provide numerical simulations showing the values of $\beta\langle\Delta E\rangle$ ($\beta > 0$) as a function of two populations of the asymptotic state for a 3LS. Notice that each point in these plots indicates a different asymptotic state, and hence a different dissipative Maxwell's demon. Depending on the specific Hamiltonian, a set of different asymptotic states may allow energy extraction from the 3LS, as indicated by the triangular checkered area. The dashed black line indicates the limit of such a region (i.e., the SSE for which $\beta\langle\Delta E\rangle = 0$). The slope of this dashed line depends on the specific Hamiltonian, and the y intercept depends on the initial inverse temperature β. In the inset in Fig. 5, we show the value of the y intercept for which the energy variation of the quantum system is zero (dashed black line) as a function of β. Thus, the checkered area represents the values of the asymptotic populations

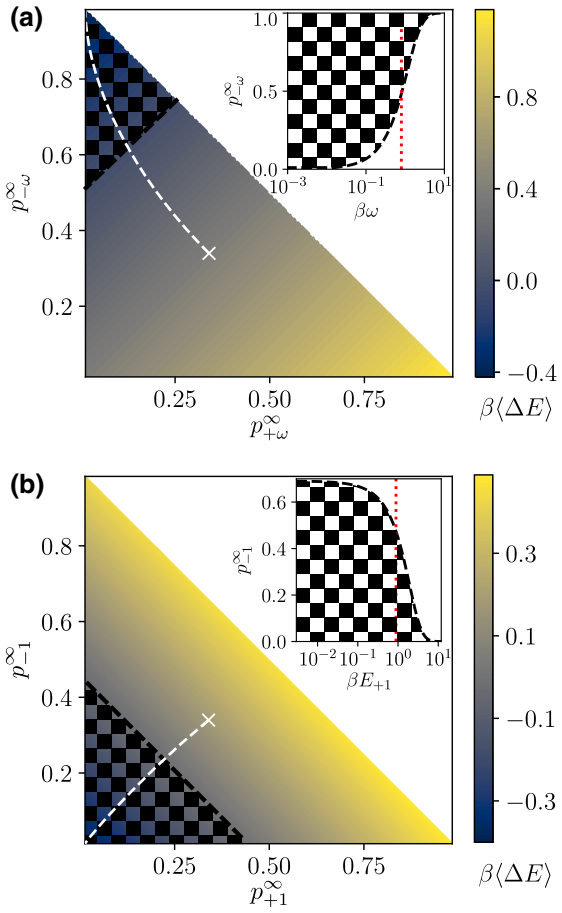

FIG. 5. Values of $\beta\langle\Delta E\rangle$ as a function of the asymptotic state populations for $\mathcal{H} = \mathcal{H}_{\mathrm{MW}}$ (a) and for $\mathcal{H} = \mathcal{H}_{\mathrm{NV}}$ (b). In these plots, each point represents a different asymptotic state of the generic quantum dissipative map Φ_d. The white cross represents a completely mixed asymptotic state for a 3LS, corresponding to the only case in which the map is unital. In addition, the subspace of thermalizing dynamics is indicated by the dashed white line, denoting that the asymptotic state is a thermal state with inverse temperature β_∞. Instead, the black line corresponds to the subspace of states for which $\beta\langle\Delta E\rangle = 0$. The checkered area corresponds to the cases where the energy of the system is reduced, $\beta\langle\Delta E\rangle < 0$ (i.e., the asymptotic states for which it is possible to extract energy from the system). Note that the inverse temperature of the initial state is fixed for each plot: (a) $\beta = 0.8/E_{+\omega}$ and (b) $\beta = 0.891/E_{+1}$. The insets show that by fixing $p^{\infty}_{+\omega} = 0$ (a) [or $p^{\infty}_{+1} = 0$ (b)], we are able to show the region where $\beta\langle\Delta E\rangle < 0$ as a function of both the asymptotic state populations and the initial inverse temperature β. Notice that β (x axis) is scaled with the highest Hamiltonian eigenvalue. The dashed red line corresponds to the value of β in (a),(b).

for which the energy variation of the system is negative. As expected, in the limit of low temperature ($\beta \to \infty$), energy extraction from the system is impossible, and the lowest-energy Hamiltonian eigenstate is the only possible SSE for which the mean energy variation is zero. In contrast, when the initial inverse temperature β approaches zero (infinite-temperature limit), the number of asymptotic states that would permit the extraction of energy is maximized.

It is worth observing that for the example considered in Fig. 5 (but also for any dissipative quantum map with a unique fixed point), the nonunitality of the underlying quantum process is a *necessary condition* for energy extraction. When the Maxwell's demon is responsible for unital dynamics, the value of the characteristic function $\mathcal{G}(\beta)$ [Eq. (13)] must be 1 for any time value and thus even asymptotically [15,57,67]. Notice though that $\gamma = 1$ does not necessarily imply that the system exhibits unital dynamics, as discussed in Appendix C. On the other hand, energy extraction is possible only when $\gamma > 1$ [15], as a consequence of Eq. (13) and Jensen's inequality. Therefore, energy extraction implies $\gamma > 1$, which in turn implies nonunital dynamics. Finally, from Fig. 5, it is apparent that energy extraction is possible for thermal asymptotic states but also for nonthermal asymptotic states.

VII. CONCLUSIONS

In this work, we use the electronic spin qutrit associated with a NV center in diamond at room temperature to realize an autonomous dissipative quantum Maxwell's demon. The interaction of the NV spin qutrit with short laser pulses is effectively described as an intrinsic feedback process, where dissipative operations (optical pumping) are applied conditioned on the result of a POVM. The demon can be effectively considered as being *autonomous*, since the feedback mechanism is inherent in the laser-induced photodynamics of the NV spin. Hence, no external agent exchanges information with the system.

We theoretically and experimentally quantify the efficacy of the demon by measuring purely quantum (non-Gibbsian) energy fluctuations, which we describe by means of an appropriate extension of the Sagawa-Ueda-Tasaki formalism for nonunitary, and even nonunital, feedback processes. For nonunital dynamics, it is not always possible to measure the efficacy, but the dissipative feature (stemming from optical pumping) of the autonomous demon allows us to measure its asymptotic value.

Finally, we also characterize the demon capability of extracting energy from the system by directly measuring the mean energy variation. We find that the efficacy is indeed a tighter bound of the mean energy variation compared with the mutual information.

Our results pave the way for the use of NV centers in diamond to further investigate open quantum system dynamics and thermodynamics. In particular, by applying cyclic interactions with the nonthermal reservoir, the possibility of creating a non-Gibbsian quantum heat engine has been conjectured [68], where quantum correlations affect the total amount of heat during the interaction processes.

More broadly, this work opens the possibility for reinterpreting dissipative phenomena, such as optical pumping, as Maxwell's demons to shed light on energy-information relations. In addition, the proposed experimental scheme to measure energy variation statistics can be adjusted to one-time measurements schemes [69–71] or to quasiprobability measurements [72] with the aim of investigating the role of coherence in energy exchange mechanisms, with the final goal of understanding the effects of genuine quantum features in thermodynamic variables. Moreover, other forms of quantum fluctuation relations based on observables that do not commute with the system Hamiltonian may be measured to explore quantum synchronization [73], and the relation of the latter with quantum mutual information and with entanglement between the quantum system and its dissipative environment. Studies of such a kind could also be performed to realize multipartite entangled systems [74] formed by single NV electronic spins and nuclear spins inside the diamond. Indeed, the high degree of control and the long coherence time for such complex spin systems would represent a very useful test bed for the relation of quantum information and quantum thermodynamics at the nanoscale.

ACKNOWLEDGMENTS

We gratefully thank Massimo Inguscio for enlightening discussions. We acknowledge financial support from the MISTI Global Seed Funds MIT-FVG Collaboration Grant and from the European Union's 2020 research and innovation program Qombs Project (FET Flagship on Quantum Technologies Grant No. 820419). S.G. also acknowledges the Blanceflor Foundation for financial support through the project entitled "The Thermodynamics behind the Measurement Postulate of Quantum Mechanics" (TRIESTE). S.H.G. acknowledges the financial support from CNR-FOE-LENS-2020.

APPENDIX A: FORMAL DERIVATION OF THE DISSIPATIVE SUT RELATION

Here we first demonstrate the validity of the general quantum fluctuation relation for an n-level quantum system under a CPTP map Φ. Then we demonstrate the validity of Eq. (13), as a corollary of the previous proof. Finally, we demonstrate the validity of the dissipative SUT relation for a dissipative map with a unique fixed point. We recall that the validity of the general quantum fluctuation relation for a CPTP map has been proved before [56–59].

Assuming a two-point-measurement scheme, the system energy is measured at the beginning of the protocol, then the system evolves under a CPTP map, and finally its energy is measured again. The Hamiltonian of the system can be decomposed in terms of the energy eigenstates that define the projectors $\mathcal{P}_i \equiv |E_i\rangle\langle E_i|$. In agreement with the superoperator formalism [60] used in Sec. III, the state after an ideal energy measurement is given by $\mathrm{col}[\mathcal{P}_i\rho\mathcal{P}_i] = \boldsymbol{\mathcal{P}}_i\mathrm{col}[\rho]$, where $\boldsymbol{\mathcal{P}}_i \equiv \mathcal{P}_i \otimes \mathcal{P}_i$. Therefore, the joint probability of obtaining E_i in the first energy measurement and E_f in the final one is written as

$$P_{f,i} = \mathrm{Tr}_{n\times n}[\boldsymbol{\mathcal{P}}_f\, \boldsymbol{\mathcal{J}}\, \boldsymbol{\mathcal{P}}_i\, \mathrm{col}[\rho^{\mathrm{th}}]], \tag{A1}$$

where ρ^{th} is the initial thermal state, $\mathrm{Tr}_{n\times n}[\mathrm{col}[\cdot]] \equiv \mathrm{Tr}[\cdot]$, and $\boldsymbol{\mathcal{J}}$ is the superoperator propagator associated with the CPTP map Φ. The characteristic function $\mathcal{G}(\beta) \equiv \langle e^{-\beta\Delta E}\rangle$ of the energy variation distribution can then be written as

$$\mathcal{G}(\beta) = \sum_{i,f=1}^{n} P_{f,i} e^{-\beta(E_f - E_i)}. \tag{A2}$$

By expressing the initial thermal state as $\rho^{\mathrm{th}} \equiv \sum_{k=1}^{n} \mathcal{P}_k e^{-\beta E_k}/Z$, with $Z \equiv \sum_{k=1}^{n} e^{-\beta E_k}$, we obtain the following:

$$\begin{aligned}\mathcal{G}(\beta) &= \sum_{i,f=1}^{n} P_{f,i} e^{-\beta(E_f - E_i)} \\ &= \sum_{i,f,k=1}^{n} \mathrm{Tr}_{n\times n}[\boldsymbol{\mathcal{P}}_f\, \boldsymbol{\mathcal{J}}\, \boldsymbol{\mathcal{P}}_i\, \mathrm{col}[\mathcal{P}_k]] e^{-\beta(E_f - E_i + E_k)}/Z \\ &= \sum_{f,k=1}^{n} \mathrm{Tr}_{n\times n}[\boldsymbol{\mathcal{P}}_f\, \boldsymbol{\mathcal{J}}\, \mathrm{col}[\mathcal{P}_k]] e^{-\beta(E_f)}/Z, \end{aligned} \tag{A3}$$

where we have used the equality $\boldsymbol{\mathcal{P}}_i\,\mathrm{col}[\mathcal{P}_k] = \mathrm{col}[\mathcal{P}_i\,\mathcal{P}_k\,\mathcal{P}_i] = \mathrm{col}[\mathcal{P}_k]\delta_{k,i}$, with $\delta_{k,i}$ the Kronecker δ. On the other hand, we know that $\mathrm{Tr}_{n\times n}[\boldsymbol{\mathcal{P}}_f\ \mathrm{col}[\rho]] = (\mathrm{col}[\mathcal{P}_f])^{\dagger}\mathrm{col}[\rho]$, for any given density matrix ρ. Hence, from Eq. (A3) we get

$$\begin{aligned}\mathcal{G}(\beta) &= \sum_{f,k=1}^{n} (\mathrm{col}[\mathcal{P}_f])^{\dagger}\, \boldsymbol{\mathcal{J}}\, \mathrm{col}[\mathcal{P}_k] e^{-\beta(E_f)}/Z \\ &= \sum_{f,k=1}^{n} (\boldsymbol{\mathcal{J}}\, \mathrm{col}[\mathcal{P}_k])^{\dagger}\ \mathrm{col}[\mathcal{P}_f] e^{-\beta(E_f)}/Z \\ &= \sum_{f,k=1}^{n} (\mathrm{col}[\mathcal{P}_k])^{\dagger}\, \boldsymbol{\mathcal{J}}^{\dagger}\, \mathrm{col}[\mathcal{P}_f] e^{-\beta(E_f)}/Z \\ &= \sum_{k=1}^{n} \mathrm{Tr}_{n\times n}[\boldsymbol{\mathcal{P}}_k\, \boldsymbol{\mathcal{J}}^{\dagger}\, \mathrm{col}[\rho_f^{\mathrm{th}}]] \qquad \text{(A4)} \\ &= \mathrm{Tr}_{n\times n}[\boldsymbol{\mathcal{J}}^{\dagger}\, \mathrm{col}[\rho_f^{\mathrm{th}}]], \qquad \text{(A5)}\end{aligned}$$

where ρ_f^{th} denotes the thermal state at inverse temperature β taking the system Hamiltonian at the time instant in which the second energy measurement of the TPM scheme is performed. In the case of a time-invariant Hamiltonian (as in the experiment in the main text) ρ_f^{th} coincides

with the initial thermal state. Equation (A5) concludes the proof.

Corollary 1: Let us assume that the quantum system is under the feedback map $\mathcal{M}_\Phi$ described in Sec. IV. Given the fact that $\mathcal{M}_\Phi$ is formed by a combination of a POVM followed by CPTP maps, it is easy to prove that the map $\mathcal{M}_\Phi$ is itself a CPTP map, such that $\mathrm{col}[\mathcal{M}_\Phi[\rho]] = \mathcal{J}_\Phi \mathrm{col}[\rho]$, with $\mathcal{J}_\Phi \equiv \sum_{k=1}^{n'} \mathbf{\Phi}_k \mathbf{\Pi}_k \mathbf{U}_0$. Therefore, using Eq. (A5), we obtain $\mathcal{G}(\beta) = \gamma = \mathrm{Tr}_{n\times n}[\sum_{k=1}^{n'} \mathbf{\Pi}_k^\dagger \mathbf{\Phi}_k^\dagger \mathrm{col}[\rho^{\mathrm{th}}]]$, hence proving the validity of Eq. (13).

Corollary 2: Assuming that the CPTP map is a dissipative map Φ_d with a unique fixed point ρ^∞, we can write $\lim_{t\to\infty} \mathcal{J}\,\mathrm{col}[\mathcal{P}_k] = \mathrm{col}[\rho^\infty]$, for every value of $k \in \{1,\ldots,n\}$. Hence, from Eq. (A4), one gets $\gamma^\infty \equiv \lim_{t\to\infty}\gamma = n\mathrm{Tr}[\rho^\infty \rho^{\mathrm{th}}]$.

Note that in the particular case of the dissipative map $\mathcal{M}$ used in our experiments, $\mathcal{J} = \mathcal{B}^{N_L}$, which describes the effect of the dissipative map after N_L laser pulses.

APPENDIX B: HAMILTONIAN EIGENSTATE PREPARATION AND FINAL READOUT GATES

As shown in Fig. 1, the preparation of the Hamiltonian initial eigenstate requires the application of the quantum gate $G_i^{(i)} : |0\rangle \to |E_i\rangle$, while the readout of the eigenstate $|E_j\rangle$ requires a second quantum gate; that is, $G_j^{-1} : |E_j\rangle \to |0\rangle$. Here we describe these gates for each of the possible states $|E_i\rangle$ and $|E_j\rangle$.

There are two possibilities for preparing the Hamiltonian eigenstates. One is with a double-driving MW gate driving transitions between $|0\rangle$ and $|\pm1\rangle$, and the other is with two MW pulses applied subsequently to transfer parts of the population from $|0\rangle$ to $|-1\rangle$ and $|+1\rangle$ separately. In our experimental setup we opt for the latter method due to easier handling of the MW operations. To induce the transition $|0\rangle \to |\emptyset\rangle \equiv 1/\sqrt{2}\,(|-1\rangle - |+1\rangle)$, the population in $|0\rangle$ has to be transferred in equal parts to $|\pm1\rangle$, where both parts have the opposite phase. This is achieved by means of a $\pi/2$ pulse that transfers half of the population to $|-1\rangle$, and a subsequent π pulse that transfers the remaining population in $|0\rangle$ to $|+1\rangle$. To obtain the correct phase between $|+1\rangle$ and $|-1\rangle$, it is required that the phase of both pulses is $\pi/2$ (or $-\pi/2$), as one can verify by calculation. Also the preparation of $|\pm\omega\rangle \equiv 1/2\left(|-1\rangle \pm \sqrt{2}\,|0\rangle + |+1\rangle\right)$ works in a very similar way. A $\pi/3$ pulse has to be applied to transfer one quarter of the population to $|-1\rangle$, and then an $\arccos(1/3)$ pulse transfers another one quarter of the population from $|0\rangle$ to $|+1\rangle$. Calculation shows that the microwave phases have to be $\mp\pi/2$ and $\pm\pi/2$, respectively, for the first and second MW pulses if we aim to prepare $|\pm\omega\rangle$.

The second quantum gate $G_j^{-1} \equiv G_j^\dagger$ applies the reverse process with respect to the preparation one. Thus, $G_2^{(j)}$ consists on applying the operations of the state preparation in reverse order and assigning to the implemented MW pulses the opposite phase.

APPENDIX C: EFFICACY OF THE DEMON AND UNITALITY WITNESS OF QUANTUM DISSIPATIVE MAPS

As mentioned in Sec. VI, $\gamma = 1$ is a consequence of unital dynamics. The opposite is not necessarily true though. Here we show how $\gamma = 1$ does not necessarily imply that the system is under unital dynamics. To do this, we focus on the case of γ^∞ [Eq. (14)], as it is a much simpler quantity than γ.

Let us take a generic n-dimensional quantum system. Notice that under the assumption that Φ_d is a dissipative map with a unique fixed point ρ^∞, which is reached asymptotically and does not depend on the initial state, the formal definition of unitality, $\Phi_d[\mathbb{1}/n] = \mathbb{1}/n$, is equivalent to

$$\Phi_d \text{ unital} \Leftrightarrow \rho^\infty = \frac{\mathbb{1}}{n}. \tag{C1}$$

On the other hand, we can write the asymptotic state after the second energy measurement, ρ^∞, according to its spectral decomposition in the $H(t=0)$ basis; that is, $\rho^\infty = \sum_{k=0}^{n-1} |E_k\rangle\langle E_k| p_k^\infty + \xi$, where ξ contains any coherent terms that may appear in the case of $[H(t=0), H(t)] \neq 0$. Using Eq. (14), one can easily show that

$$\gamma^\infty = 1 \Leftrightarrow \sum_{k=1}^{n-1}\left(p_k^\infty - \frac{1}{n}\right)\left(e^{-\beta E_0} - e^{-\beta E_k}\right) = 0. \tag{C2}$$

Clearly, the state $\rho^\infty = \mathbb{1}/n$ is a solution of Eq. (C2), but it is not the only one. There is a whole family of solutions given by the condition

$$p_{n-1}^\infty = \frac{1}{n} - \sum_{k=1}^{n-2}\left(p_k^\infty - \frac{1}{n}\right)\left(\frac{e^{-\beta E_0} - e^{-\beta E_k}}{e^{-\beta E_0} - e^{-\beta E_{n-1}}}\right). \tag{C3}$$

Notice though that if ρ^∞ is constrained to be a thermal state (thermalizing dynamics), then the only solution is indeed $\rho^\infty = \mathbb{1}/n$.

[1] K. Maruyama, F. Nori, and V. Vedral, Colloquium: The physics of Maxwell's demon and information, Rev. Mod. Phys. **81**, 1 (2009).

[2] C. Bennett, The thermodynamics of computation—a review, Int. J. Theor. Phys. **21**, 905 (1982).

[3] K. Funo, M. Ueda, and T. Sagawa, *Thermodynamics in the Quantum Regime - Fundamental Aspects and New Directions* (Springer International Publishing, Cham, Switzerland, 2018), p. 249.

[4] J. V. Koski, V. F. Maisi, T. Sagawa, and J. P. Pekola, Experimental Observation of the Role of Mutual Information in the Nonequilibrium Dynamics of a Maxwell Demon, Phys. Rev. Lett. **113**, 030601 (2014).

[5] M. Naghiloo, J. J. Alonso, A. Romito, E. Lutz, and K. W. Murch, Information Gain and Loss for a Quantum Maxwell's Demon, Phys. Rev. Lett. **121**, 030604 (2018).

[6] D. Mandal and C. Jarzynski, Work and information processing in a solvable model of Maxwell's demon, Proc. Nat. Acad. Sc. **109**, 1 (2012).

[7] A. Kutvonen, J. Koski, and T. Ala-Nissila, Thermodynamics and efficiency of an autonomous on-chip Maxwell's demon, Sci. Rep. **6**, 21126 (2016).

[8] L. Buffoni, A. Solfanelli, P. Verrucchi, A. Cuccoli, and M. Campisi, Quantum Measurement Cooling, Phys. Rev. Lett. **122**, 070603 (2019).

[9] C. Elouard, D. A. Herrera-Martí, M. Clusel, and A. Auffeves, The role of quantum measurement in stochastic thermodynamics, Npj Quantum Inf. **3**, 9 (2017).

[10] S. Gherardini, L. Buffoni, M. M. Müller, F. Caruso, M. Campisi, A. Trombettoni, and S. Ruffo, Nonequilibrium quantum-heat statistics under stochastic projective measurements, Phys. Rev. E **98**, 032108 (2018).

[11] S. Toyabe, T. Sagawa, M. Ueda, E. Muneyuki, and M. Sano, Experimental demonstration of information-to-energy conversion and validation of the generalized Jarzynski equality, Nat. Phys. **6**, 988 (2010).

[12] Y. Masuyama, K. Funo, Y. Murashita, A. Noguchi, S. Kono, Y. Tabuchi, R. Yamazaki, M. Ueda, and Y. Nakamura, Information-to-work conversion by maxwell's demon in a superconducting circuit quantum electrodynamical system, Nat. Commun. **9**, 1291 (2018).

[13] J. V. Koski, A. Kutvonen, I. M. Khaymovich, T. Ala-Nissila, and J. P. Pekola, On-Chip Maxwell's Demon as an Information-Powered Refrigerator, Phys. Rev. Lett. **115**, 260602 (2015).

[14] C. Elouard, D. Herrera-Martí, B. Huard, and A. Auffèves, Extracting Work from Quantum Measurement in Maxwell's Demon Engines, Phys. Rev. Lett. **118**, 260603 (2017).

[15] M. Campisi, J. Pekola, and R. Fazio, Feedback-controlled heat transport in quantum devices: Theory and solid-state experimental proposal, New J. Phys. **19**, 053027 (2017).

[16] P. Schindler, J. T. Barreiro, T. Monz, V. Nebendahl, D. Nigg, M. Chwalla, M. Hennrich, and R. Blatt, Experimental repetitive quantum error correction, Science **332**, 1059 (2011).

[17] M. Hirose and P. Cappellaro, Coherent feedback control of a single qubit in diamond, Nature **532**, 77 (2016).

[18] P. A. Camati, J. P. S. Peterson, T. B. Batalhão, K. Micadei, A. M. Souza, R. S. Sarthour, I. S. Oliveira, and R. M. Serra, Experimental Rectification of Entropy Production by Maxwell's Demon in a Quantum System, Phys. Rev. Lett. **117**, 240502 (2016).

[19] M. D. Vidrighin, O. Dahlsten, M. Barbieri, M. S. Kim, V. Vedral, and I. A. Walmsley, Photonic Maxwell's Demon, Phys. Rev. Lett. **116**, 050401 (2016).

[20] N. Cottet, S. Jezouin, L. Bretheau, P. Campagne-Ibarcq, Q. Ficheux, J. Anders, A. Auffèves, R. Azouit, P. Rouchon, and B. Huard, Observing a quantum Maxwell demon at work, PNAS **114**, 7561 (2017).

[21] X. Song, M. Naghiloo, and K. Murch, Quantum process inference for a single-qubit Maxwell demon, Phys. Rev. A **104**, 022211 (2021).

[22] W. Ji, Z. Chai, M. Wang, Y. Guo, X. Rong, F. Shi, C. Ren, Y. Wang, and J. Du, Spin Quantum Heat Engine Quantified by Quantum Steering, Phys. Rev. Lett. **128**, 090602 (2022).

[23] B.-L. Najera-Santos, P. A. Camati, V. Métillon, M. Brune, J.-M. Raimond, A. Auffèves, and I. Dotsenko, Autonomous maxwell's demon in a cavity qed system, Phys. Rev. Res. **2**, 032025 (2020).

[24] F. Verstraete, M. M. Wolf, and J. I. Cirac, Quantum computation and quantum-state engineering driven by dissipation, Nat. Phys. **5**, 633 (2009).

[25] F. Pastawski, L. Clemente, and J. Ignacio Cirac, Quantum memories based on engineered dissipation, Phys. Rev. A **83**, 012304 (2011).

[26] V. Scarani, M. Ziman, P. Štelmachovič, N. Gisin, and V. Bužek, Thermalizing Quantum Machines: Dissipation and Entanglement, Phys. Rev. Lett. **88**, 097905 (2002).

[27] R. Nandkishore and D. A. Huse, Many-body localization and thermalization in quantum statistical mechanics, Annu. Rev. Condens. Matter Phys. **6**, 15 (2015).

[28] P. Strasberg, G. Schaller, T. Brandes, and M. Esposito, Quantum and Information Thermodynamics: A Unifying Framework Based on Repeated Interactions, Phys. Rev. X **7**, 021003 (2017).

[29] J. T. Barreiro, M. Müller, P. Schindler, D. Nigg, T. Monz, M. Chwalla, M. Hennrich, C. F. Roos, P. Zoller, and R. Blatt, An open-system quantum simulator with trapped ions, Nature **470**, 486 (2011).

[30] H.-V. Do, C. Lovecchio, I. Mastroserio, N. Fabbri, F. S. Cataliotti, S. Gherardini, M. M. Müller, N. Dalla Pozza, and F. Caruso, Experimental proof of quantum zeno-assisted noise sensing, New J. Phys. **21**, 113056 (2019).

[31] S. P. Wolski, D. Lachance-Quirion, Y. Tabuchi, S. Kono, A. Noguchi, K. Usami, and Y. Nakamura, Dissipation-Based Quantum Sensing of Magnons with a Superconducting Qubit, Phys. Rev. Lett. **125**, 117701 (2020).

[32] Y. Xie, J. Geng, H. Yu, X. Rong, Y. Wang, and J. Du, Dissipative Quantum Sensing with a Magnetometer Based on Nitrogen-Vacancy Centers in Diamond, Phys. Rev. Appl. **14**, 014013 (2020).

[33] Y. Lin, J. P. Gaebler, F. Reiter, T. R. Tan, R. Bowler, A. S. Sørensen, D. Leibfried, and D. J. Wineland, Dissipative production of a maximally entangled steady state of two quantum bits, Nature **504**, 415 (2013).

[34] G. Barontini, L. Hohmann, F. Haas, J. Estève, and J. Reichel, Deterministic generation of multiparticle entanglement by quantum zeno dynamics, Science **349**, 1317 (2015).

[35] A. Biella, F. Storme, J. Lebreuilly, D. Rossini, R. Fazio, I. Carusotto, and C. Ciuti, Phase diagram of incoherently driven strongly correlated photonic lattices, Phys. Rev. A **96**, 023839 (2017).

[36] Y. Lu, S. Chakram, N. Leung, N. Earnest, R. K. Naik, Z. Huang, P. Groszkowski, E. Kapit, J. Koch, and

D. I. Schuster, Universal Stabilization of a Parametrically Coupled Qubit, Phys. Rev. Lett. **119**, 150502 (2017).
[37] R. Ma, B. Saxberg, C. Owens, N. Leung, Y. Lu, and J. Simon, and D. I. Schuster, A dissipatively stabilized mott insulator of photons, Nature **566**, 51 (2019).
[38] F. Benatti and R. Floreanini, *Irreversible Quantum Dynamics* (Springer Science & Business Media, Heidelberg, Germany, 2003), Vol. 622.
[39] S. Dutta and N. R. Cooper, Out-of-equilibrium steady states of a locally driven lossy qubit array, Phys. Rev. Res. **3**, L012016 (2021).
[40] N. Gisin, Quantum Measurements and Stochastic Processes, Phys. Rev. Lett. **52**, 1657 (1984).
[41] K. Jacobs, *Quantum Measurement Theory and its Applications* (Cambridge University Press, Cambridge, UK, 2014).
[42] M. Esposito, U. Harbola, and S. Mukamel, Nonequilibrium fluctuations, fluctuation theorems, and counting statistics in quantum systems, Rev. Mod. Phys. **81**, 1665 (2009).
[43] M. Campisi, P. Hänggi, and P. Talkner, Colloquium: Quantum fluctuation relations: Foundations and applications, Rev. Mod. Phys. **83**, 771 (2011).
[44] S. An, J.-N. Zhang, M. Um, D. Lv, Y. Lu, J. Zhang, Z.-Q. Yin, H. T. Quan, and K. Kim, Experimental test of the quantum Jarzynski equality with a trapped-ion system, Nat. Phys. **11**, 193 (2015).
[45] A. Smith, Y. Lu, S. An, X. Zhang, J.-N. Zhang, Z. Gong, H. T. Quan, C. Jarzynski, and K. Kim, Verification of the quantum nonequilibrium work relation in the presence of decoherence, New J. Phys. **20**, 013008 (2018).
[46] T. B. Batalhão, A. M. Souza, L. Mazzola, R. Auccaise, R. S. Sarthour, I. S. Oliveira, J. Goold, G. De Chiara, M. Paternostro, and R. M. Serra, Experimental Reconstruction of Work Distribution and Study of Fluctuation Relations in a Closed Quantum System, Phys. Rev. Lett. **113**, 140601 (2014).
[47] S. Pal, T. S. Mahesh, and B. K. Agarwalla, Experimental demonstration of the validity of the quantum heat-exchange fluctuation relation in an nmr setup, Phys. Rev. A **100**, 042119 (2019).
[48] F. Cerisola, Y. Margalit, S. Machluf, A. Roncaglia, J. Paz, and R. Folman, Using a quantum work meter to test non-equilibrium fluctuation theorems, Nat. Commun. **8**, 1241 (2017).
[49] Z. Zhang, T. Wang, L. Xiang, Z. Jia, P. Duan, W. Cai, Z. Zhan, Z. Zong, J. Wu, L. Sun, Y. Yin, and G. Guo, Experimental demonstration of work fluctuations along a shortcut to adiabaticity with a superconducting xmon qubit, New J. Phys. **20**, 085001 (2018).
[50] S. Hernández-Gómez, S. Gherardini, F. Poggiali, F. S. Cataliotti, A. Trombettoni, P. Cappellaro, and N. Fabbri, Experimental test of exchange fluctuation relations in an open quantum system, Phys. Rev. Res. **2**, 023327 (2020).
[51] P. H. S. Ribeiro, T. Häffner, G. L. Zanin, N. R. da Silva, R. M. de Araújo, W. C. Soares, R. J. de Assis, L. C. Céleri, and A. Forbes, Experimental study of the generalized jarzynski fluctuation relation using entangled photons, Phys. Rev. A **101**, 052113 (2020).
[52] T. Sagawa and M. Ueda, Second law of Thermodynamics with Discrete Quantum Feedback Control, Phys. Rev. Lett. **100**, 080403 (2008).
[53] Y. Morikuni and H. Tasaki, Quantum jarzynski-sagawa-ueda relations, J. Stat. Phys. **143**, 1 (2011).
[54] K. Funo, Y. Watanabe, and M. Ueda, Integral quantum fluctuation theorems under measurement and feedback control, Phys. Rev. E **88**, 052121 (2013).
[55] K. Funo, Y. Murashita, and M. Ueda, Quantum nonequilibrium equalities with absolute irreversibility, New J. Phys. **17**, 075005 (2015).
[56] D. Kafri and S. Deffner, Holevo's bound from a general quantum fluctuation theorem, Phys. Rev. A **86**, 044302 (2012).
[57] A. E. Rastegin, Non-equilibrium equalities with unital quantum channels, J. Stat. Mech. **2013**, P06016 (2013).
[58] T. Albash, D. A. Lidar, M. Marvian, and P. Zanardi, Fluctuation theorems for quantum processes, Phys. Rev. E **88**, 032146 (2013).
[59] J. Goold, M. Paternostro, and K. Modi, Nonequilibrium Quantum Landauer Principle, Phys. Rev. Lett. **114**, 060602 (2015).
[60] T. F. Havel, Robust procedures for converting among lindblad, kraus and matrix representations of quantum dynamical semigroups, J. Math. Phys. **44**, 534 (2003).
[61] M. Steiner, P. Neumann, J. Beck, F. Jelezko, and J. Wrachtrup, Universal enhancement of the optical readout fidelity of single electron spins at nitrogen-vacancy centers in diamond, Phys. Rev. B **81**, 035205 (2010).
[62] M. W. Doherty, N. B. Manson, P. Delaney, F. Jelezko, J. Wrachtrup, and L. C. L. Hollenberg, The nitrogen-vacancy colour centre in diamond, Phys. Rep. **528**, 1 (2013).
[63] J. Wolters, M. Strauß, R. S. Schoenfeld, and O. Benson, Quantum zeno phenomenon on a single solid-state spin, Phys. Rev. A **88**, 020101 (2013).
[64] P. Talkner, E. Lutz, and P. Hänggi, Fluctuation theorems: Work is not an observable, Phys. Rev. E **75**, 050102 (2007).
[65] A. E. Rastegin and K. Życzkowski, Jarzynski equality for quantum stochastic maps, Phys. Rev. E **89**, 012127 (2014).
[66] V. Cimini, S. Gherardini, M. Barbieri, I. Gianani, M. Sbroscia, L. Buffoni, M. Paternostro, and F. Caruso, Experimental characterization of the energetics of quantum logic gates, Npj Quantum Inf. **6**, 96 (2020).
[67] G. Guarnieri, S. Campbell, J. Goold, S. Pigeon, B. Vacchini, and M. Paternostro, Full counting statistics approach to the quantum non-equilibrium landauer bound, New J. Phys. **19**, 103038 (2017).
[68] B. Gardas and S. Deffner, Thermodynamic universality of quantum carnot engines, Phys. Rev. E **92**, 042126 (2015).
[69] S. Gherardini, A. Belenchia, M. Paternostro, and A. Trombettoni, End-point measurement approach to assess quantum coherence in energy fluctuations, Phys. Rev. A **104**, L050203 (2021).
[70] K. Micadei, G. T. Landi, and E. Lutz, Quantum Fluctuation Theorems beyond Two-Point Measurements, Phys. Rev. Lett. **124**, 090602 (2020).
[71] A. Sone, Y.-X. Liu, and P. Cappellaro, Quantum Jarzynski Equality in Open Quantum Systems from the One-Time Measurement Scheme, Phys. Rev. Lett. **125**, 060602 (2020).
[72] A. Levy and M. Lostaglio, Quasiprobability distribution for heat fluctuations in the quantum regime, PRX Quantum **1**, 010309 (2020).

[73] A. Roulet and C. Bruder, Quantum Synchronization and Entanglement Generation, Phys. Rev. Lett. **121**, 063601 (2018).

[74] M. H. Abobeih, J. Randall, C. E. Bradley, H. P. Bartling, M. A. Bakker, M. J. Degen, M. Markham, D. J. Twitchen, and T. H. Taminiau, Atomic-scale imaging of a 27-nuclear-spin cluster using a quantum sensor, Nature **576**, 411 (2019).

[75] See Supplemental Material at http://link.aps.org/supplemental/10.1103/PRXQuantum.3.020329.